

1 Changes in global teleconnection patterns under global warming and stratospheric aerosol  
2 intervention scenarios

3 **Abolfazl Rezaei<sup>1,2</sup>, Khalil Karami<sup>3</sup>, Simone Tilmes<sup>4</sup>, & John C. Moore<sup>5, 6, 7</sup>**

4  
5 <sup>1</sup> Department of Earth Sciences, Institute for Advanced Studies in Basic Sciences, Zanjan 45137–  
6 66731, Iran. [arezaei@iasbs.ac.ir](mailto:arezaei@iasbs.ac.ir); [abolfazlrezaei64@gmail.com](mailto:abolfazlrezaei64@gmail.com).

7 <sup>2</sup> Center for Research in Climate Change and Global Warming (CRCC), Institute for Advanced Studies  
8 in Basic Sciences (IASBS), Zanjan 45137–66731, Iran.

9 <sup>3</sup> Institut für Meteorologie, Stephanstraße 3, 04103 Leipzig, Germany. [khalil.karami@uni-leipzig.de](mailto:khalil.karami@uni-leipzig.de)

10 <sup>4</sup> National Center for Atmospheric Research, Boulder, CO, USA. [tilmes@ucar.edu](mailto:tilmes@ucar.edu)

11 <sup>5</sup> College of Global Change and Earth System Science, Beijing Normal University, Beijing, 100875,  
12 China. [john.moore.bnu@gmail.com](mailto:john.moore.bnu@gmail.com)

13 <sup>6</sup> CAS Center for Excellence in Tibetan Plateau Earth Sciences, Beijing, 100101, China.

14 <sup>7</sup> Arctic Centre, University of Lapland, Rovaniemi, 96101, Finland.

15  
16 **Abstract**

17 We investigate the potential impact of Stratospheric Aerosol Intervention (SAI) on the  
18 spatiotemporal behavior of large-scale climate teleconnection patterns represented by the North  
19 Atlantic Oscillation (NAO), Pacific Decadal Oscillation (PDO), El Niño/Southern Oscillation (ENSO)  
20 and Atlantic Multidecadal Oscillation (AMO) indices using simulations from the Community Earth  
21 System Models (CESM1 and CESM2). The leading Empirical Orthogonal Function of sea surface  
22 temperature (SST) anomalies indicates that greenhouse gas (GHG) forcing is accompanied by  
23 increases in variance across both the North Atlantic (i.e., AMO) and North Pacific (i.e., PDO) and a  
24 decrease over the tropical Pacific (i.e., ENSO); however, SAI effectively reverses these global  
25 warming-imposed changes. The projected spatial patterns of SST anomaly related to ENSO show no  
26 significant change under either global warming or SAI. In contrast, the spatial anomaly patterns  
27 pertaining to AMO (i.e., in the North Atlantic) and PDO (i.e., in the North Pacific) changes under global  
28 warming are effectively suppressed by SAI. For AMO, the low contrast between the cold-tongue  
29 pattern and its surroundings in the North Atlantic, predicted under global warming, is restored under  
30 SAI scenarios to similar patterns as in the historical period. The frequencies of El Niño and La Niña  
31 episodes modestly- increase with GHG greenhouse gas emissions in CESM2the models, while SAI  
32 tends to compensate for them. All climate indices' dominant modes of inter-annual variability are  
33 projected to be preserved in both warming and SAI scenarios. However, the dominant decadal and

34 interdecadal variability mode changes induced by global warming are exacerbated by SAI,  
35 particularly in the Atlantic-based AMO. Nonetheless, these findings are limited by the data available,  
36 especially for multi-decadal signals, with less than 100-year long simulations available for SAI.

37 **Keywords:** Ocean-atmosphere teleconnection patterns; GLENS; SSP5-85; Stratospheric Aerosol  
38 Intervention; Global warming

39

#### 40 **500-character non-technical text**

41 Teleconnection patterns are important characteristics of the climate system, well-known examples  
42 include the El Niño and La Niña events driven from the tropical Pacific. We examined how patterns  
43 that arise in the Pacific and Atlantic Oceans behave under stratospheric aerosol geoengineering and  
44 greenhouse gas (GHG)-induced warming. In general, geoengineering reverses trends, however in the  
45 Atlantic, the multidecadal oscillations that are-is shifted to higher frequencies by GHG greenhouse  
46 gas-are is further strengthened.

47

#### 48 **1. Introduction**

49 Although the Paris agreement and accompanying international commitments to decrease carbon  
50 emissions are an essential step forward, current nationally contributions have only about a 50%  
51 chance to restrict global mean temperature increase to 2°C above preindustrial (Meinshausen et al.,  
52 2022). Exceeding 2°C will lead to severe consequences and societal disruption worldwide as  
53 humanity is critically dependent on ecosystems, food, fresh water, and health systems which face  
54 rapidly challenging adaptation pressure above 2°C of global warming (Field and Barros, 2014).

55 In parallel with emissions reductions, solar radiation modification (SRM) has been suggested to limit  
56 global temperature increases and consequent climate impacts from anthropogenic greenhouse gas  
57 (GHG) emissions. A naturally occurring analog of SRM is the well-known global surface cooling  
58 following large volcanic eruptions, albeit over relatively short periods. Simulations have shown that  
59 SRM decreasing total solar irradiance by about 2%, would roughly compensate for global warming  
60 from a doubling of CO<sub>2</sub> concentrations (Dagon and Schrag, 2016).

61 Oceans act as major drivers of climate variability worldwide (e.g., Shukla, 1998; Cai et al., 2021), and  
62 more than 90% of the excess energy balance of the earth arising from GHG greenhouse gas emissions  
63 ends up heating the ocean (Cheng et al., 2015). Variations in sea surface temperatures (SSTs) and the  
64 global climate are linked through ocean-atmosphere energy exchanges that can be helpfully  
65 summarized by climate indices that characterize large-scale climate teleconnection patterns. That is  
66 recurring and persistent, large-scale anomaly patterns of pressure and circulation across large

67 geographical regions. Some of the most referred to are El Niño/Southern Oscillation (ENSO), Pacific  
68 Decadal Oscillation (PDO), Atlantic Multidecadal Oscillation (AMO), and North Atlantic Oscillation  
69 (NAO). The dominant inter-annual feature of climate variability on the planet is ENSO, and its state  
70 produces widespread climatic and environmental outcomes (Latif and Keenlyside, 2009). The PDO  
71 modulates marine ecosystems and global climate on decadal time scales (Mantua et al., 1997),  
72 impacts ENSO onset and frequency (Fang et al., 2014), and is useful for short- to long-term climate  
73 forecast (An and Wang, 1999). The AMO has broader hemispheric impacts beyond North American  
74 and European climates (Enfield et al. 2001), influencing the monsoons across North African, East  
75 Asia, and India (Zhang and Delworth 2006). The NAO is among the dominant climate variability  
76 modes in the northern hemisphere (Simpkins, 2021).

77 Several studies have explored how climate indices, particularly ENSO, respond to global warming  
78 and increasing ~~GHG greenhouse gas~~ concentrations. Statistically significant systemic changes have  
79 occurred in ENSO dynamics and the evolution of El Niño and La Niña events since the 1960s (Moron  
80 et al., 1998; Capotondi and Sardeshmukh, 2017). ENSO may favor more severe events under global  
81 warming (Fedorov and Philander, 2001), and Cai et al. (2015) found that ENSO-associated disastrous  
82 weather consequences tend to arise more frequently under unabated CO<sub>2</sub> emissions. Cai et al. (2021)  
83 found an inter-model consensus on increases in forthcoming ENSO rainfall and temperature  
84 fluctuations under increasing ~~GHG greenhouse gas~~ concentrations. The PDO, which is essentially the  
85 extra-tropical manifestation of ENSO, is simulated with a similar spatial pattern as at present under  
86 various future climates but with reduced amplitude and a shorter characteristic time scale (e.g.,  
87 Zhang and Delworth, 2016). The North Atlantic is a key ocean for investigating global climate  
88 changes (Wang and Dong, 2010), and acts as a major carbon dioxide sink (Watson et al., 2009).  
89 Atmospheric CO<sub>2</sub> concentrations vary with the phase of the AMO with the warm phase associated  
90 with lowered atmospheric CO<sub>2</sub> (Wang and Dong, 2010). The two NAO action points in the Icelandic  
91 low and the Azores high have been projected to significantly intensify and shift northeastward by 10-  
92 to-20° in latitude and 30-to-40° in longitude in response to global warming (Hu and Wu, 2004).

93 Stratospheric Aerosol Intervention (SAI), is a type of SRM that has been widely simulated by many  
94 global climate models (e.g., Kravitz et al., 2013), which is accompanied by changing in global  
95 circulations such as the NAO teleconnection pattern (Moore et al., 2014), and is known in various  
96 models to partially offset the decline in the Atlantic Meridional Overturning Circulation (AMOC; Xie  
97 et al., 2022). Undorf et al. (2018) simulated the North Atlantic SST cooling accompanied by the  
98 historical rise of stratospheric sulfate aerosol from North America and Europe dating back to 1850-  
99 1975. Gabriel and Robock (2015) is the only study to date that explores the effects of SAI in multiple

100 models on the possible amplitude and frequency changes of El Niño/Southern Oscillation (ENSO).  
101 They concluded that changes in ENSO in the SAI simulations were either not present or not large  
102 enough to be captured by their approach, given the across-model variability issue. Thus, little is  
103 known about possible changes that future global climate change scenarios with artificial cooling may  
104 have on ocean-atmosphere climate indices. Recently, a novel set of SRM models have been globally  
105 complete with the state-of-the-art climate models: Community Earth System Model versions 1 and  
106 2 (CESM1 and CESM2). These models have improved planetary boundary layer turbulence, aerosols,  
107 radiation, and cloud microphysics which should enable more reliable for the forthcoming global  
108 climate change projections (Mills et al., 2017).

109 We use the Geoengineering Large Ensemble Simulation (GLENS) with 20 members from a single  
110 model, the Community Earth System Model 1 (CESM1) with Stratospheric Aerosol Intervention  
111 (GLENS-SAI), to explore the possible changes in climate teleconnection patterns under future climate  
112 change scenarios. The models use the Representative Concentration Pathway (RCP) 8.5 high GHG  
113 greenhouse gas emissions forcing state (Riahi et al., 2011) as a baseline and increase stratospheric  
114 sulfur injections through the century, to maintain global surface temperatures at 2020 levels. This  
115 produces an increasingly large signal-to-noise ratio through the 21<sup>st</sup> century. In addition, we use  
116 recent simulations (SSP5-8.5-SAI) with an updated model version (CESM2). For these simulations,  
117 the SSP5-8.5 GHG greenhouse gas emissions scenarios were used as the GHG greenhouse gas baseline  
118 scenario on which SAI was performed. The two different model experiments show some surprising  
119 differences in the required sulfur injections and climate outcomes with and without SAI applications  
120 (~~Tilmes et al., 2020~~, Fasullo et al., 2020, Tilmes et al., 2020). Thus, even models from different  
121 generations in the same family can produce sufficiently different climates to explore a range of  
122 plausibly real climate impacts. The goal of this study is to identify robust features across the two  
123 model versions in the response of climate indices (ENSO, PDO, AMO and NAO) to GHG greenhouse  
124 gas induced global warming and its compensation by SAI.

125 We employed empirical orthogonal functions and wavelet transforms to decompose time series and  
126 study the differences in the climate teleconnection indices patterns between the SSP5-8.5 and SSP5-  
127 8.5-SAI scenarios. Since teleconnection patterns are emergent features of the non-linear, chaotic  
128 climate system (Ghil et al., 2002), their underlying physical causes are complex and not necessarily  
129 the same in any model as on the real planet. Hence, we assess the potential changes in temporal and  
130 spatial characteristics of climate indices of AMO, NAO, ENSO, and PDO under both extreme warming  
131 GHG greenhouse scenarios and with SAI employed to mitigate those warmings while maintaining  
132 extreme GHG greenhouse gas concentration trajectories.

133

## 134 2. Data and Methods

### 135 2.1. Models and scenarios

136 We used two SAI models and scenarios: (1) CESM1 for GLENS-SAI and (2) CESM2 for SSP5-8.5-SAI.

137 The GLENS (~~Geoengineering Large Ensemble~~) project used the RCP8.5 as a baseline scenario (Tilmes

138 ~~et al., 2018~~). Simulations were done by the Community Earth System Model version 1 (CESM1) with

139 the Whole Atmosphere Community Climate Model (WACCM) as the atmospheric system integrated

140 to land, ocean, and sea ice models (Mills et al., 2017). The resolution of atmospheric component is

141 1.25° in longitude and 0.9° in latitude. A 20-member reference simulation for the RCP8.5 scenario

142 (Riahi et al., 2011) over the 2010–2030 period with three ensemble members (001 to 003)

143 continuing up to the end of the 21<sup>st</sup> century. GLENS-SAI is a 20-member ensemble of stratospheric

144 sulfur dioxide (SO<sub>2</sub>) injection simulations, spanning 2020-2099. ~~This experiment was designed to~~

145 ~~keep the mean surface temperature at 2020 global conditions, and also stabilize interhemispheric~~

146 ~~and equator to pole surface temperature gradients at 2020 values while forced by the RCP8.5~~

147 ~~greenhouse gas scenario. Stratospheric injections were performed at four different latitudes (15°N~~

148 ~~and 15°S at 25 km, 30°N and 30°S), at 22.8 km, and at 180° longitude using a feedback control~~

149 ~~algorithm (Kravitz et al., 2017; Tilmes et al., 2018)~~. Each ensemble member was begun in 2010 with

150 small differences in their initial air temperatures, while their ocean, sea-ice, and land temperatures

151 were the same. Even before the start of the SAI injections in 2020, the fully coupled model produced

152 variability between the ensemble members due to its chaotic nature. Here, we use all available

153 members of the RCP8.5 and GLENS-SAI simulations, which extend until the end of the 21<sup>st</sup> century.

154 For the analysis, we used monthly SST and sea-level pressure (PSL).

155 We also analyzed output from the NCAR Community Earth System Model version 2- Whole

156 Atmosphere Community Climate Model Version 6 (CESM2(WACCM6)). This model version was used

157 for performing the Coupled Model Intercomparison Project Phase 6 (CMIP6; Eyring et al., 2016)

158 simulations. Like GLENS, this SAI experiment is according to the high ~~GHG~~greenhouse gas emissions

159 scenario, called SSP5-85 in CMIP6, (SSP5-8.5-SAI) and limits mean global temperatures to 1.5°C

160 above 1850–1900 conditions, which without SAI, is exceeded around the year 2020 in

161 CESM2(WACCM6) under SSP5-8.5. The experiment used sulfur injection locations at the same four

162 latitudes as in GLENS to accomplish the same three temperature goals (Tilmes et al., 2020). We used

163 the monthly SST and PSL data from all five members (r1 to r5) of the SSP5-8.5 scenario (covering

164 2015-2100) and the three available ensemble members of SSP5-8.5-SAI that cover the period of

165 2020-2100. For the analysis, we also applied a one-member historical simulation based on the

166 specific CESM1(WACCM) version used for GLENS between 1980-2009 (denoted as “historical” in the  
167 following). All three corresponding members (r1 to r3) from the CESM2(WACCM6) version were  
168 used for the historical period.

169 The SAI scenarios using both CESM1 and CESM2 inject SO<sub>2</sub> at four predefined points (30°N, 30°S,  
170 15°N, and 15°S) at ~5 km above the tropopause using a feedback controller to maintain not just the  
171 global mean temperature, but the interhemispheric and equator-to-pole temperature gradients.  
172 Fasullo and Richter (2022) explain the inter-model differences in the aerosol mass latitudinal  
173 distributions between the SAI experiments using CESM1 and CESM2. CESM2 SAI utilizes the CMIP6  
174 SSP5-8.5 experiment as a baseline which has been used by various modeling teams (Tilmes et al.,  
175 2020) while CESM1 SAI uses the well-known RCP8.5 scenario. In GLENS-SAI, most of the aerosols  
176 were injected at 30°N and 30°S with much smaller injection mass at 15°N and a tiny amount at 15°S  
177 while for SSP5-8.5-SAI, the highest concentrations were released at 15°S, modest mass at 15°N and  
178 30°S, and a small amount at 30°N. These differences in the SO<sub>2</sub> distributions across the two SAI  
179 scenarios for CESM1 and CESM2 produce a range of variability in shortwave radiation and cloud  
180 responses to CO<sub>2</sub> concentration increases (Fasullo and Richter, 2022). Additionally, Fasullo and  
181 Richter (2022) identified that changes in the spatial salinity and density patterns in the Atlantic  
182 Ocean, and in turn, the Atlantic Meridional Overturning Circulation (AMOC), are very different under  
183 GLENS-SAI compared to SSP5-8.5-SAI experiment. These differences between SAI simulations  
184 represent part of the system variability.

185 The equilibrium climate sensitivity (ECS) of CESM2-WACCM is 4.75 °C and lies in an ECS range of 1.83  
186 to 5.67 °C from 41 different CMIP6 GCMs (IPCC AR6, 2021). The absolute mean surface temperature  
187 difference between CESM2-WACCM and historical records (0.89 °C) and is also within the range of  
188 0.38-1.23 °C from 37 different CMIP6 models (Scafetta, 2021). CESM2 is one of the best nine models  
189 for simulating precipitation worldwide when measured by the Hellinger distance between bivariate  
190 empirical densities of 34 CMIP6 models and the historical data from Global Precipitation Climatology  
191 Centre (GPCC; Abdelmoaty et al., 2021). Additionally, the global-mean values of SST, summer land  
192 temperatures, precipitation, and ECS simulated by CESM1 and CESM2 are roughly similar to each  
193 other as well as compatible with the historical values over the 1985-2014 period (Danabasoglu et al.,  
194 2020; Table S1).

195 Relative to the preindustrial 1851-1850 period, CESM2-WACCM projects global mean surface air  
196 temperature rises of ~6.25 °C by the 2071-2100 period under SSP5-8.5 which compares with the  
197 range of ~3.3-6.6 °C from 35 ensembles of 12 CMIP6 models (Cook et al., 2020).

198

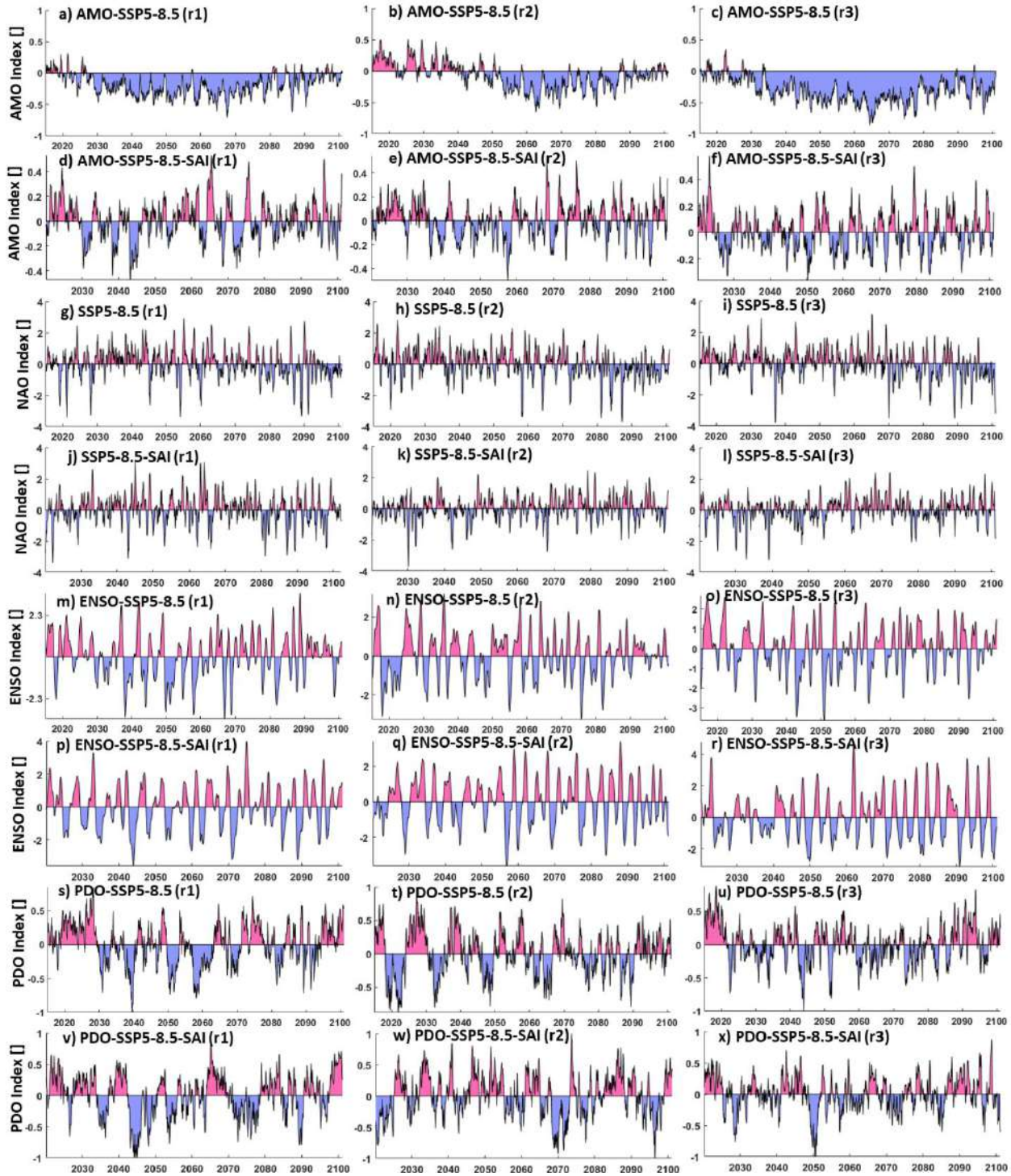
199 **2.2. Climate indices**

200 The AMO was calculated from the area-weighted average of SSTs across the northern Atlantic from  
201 0-70° N. The NAO was computed from the PSL time series at two stations: Gibraltar (to the south of  
202 Spain; around 36.1°N and 5.3°W) and Reykjavik (in the southwest of Iceland; around 64.1°N and  
203 22.0°W). The ENSO index follows the definition proposed by Trenberth (1997). Here, we used SSTs  
204 at the Niño 3.4 region (east-central equatorial Pacific between 5°N-5°S, 170°W-120°W) as a proxy  
205 for ENSO. After removing the global mean SST anomaly, the leading Empirical Orthogonal Function  
206 (EOF) of monthly SST anomalies across the North Pacific (20°-70°N) is termed PDO following Mantua  
207 et al. (1997). All these computations were analyzed through the Climate Data Toolbox prepared by  
208 Greene et al. (2019). As an example, Fig. 1 compares AMO, NAO, ENSO, and PDO indices obtained  
209 from SSP5-8.5 and SSP5-8.5-SAI scenarios.

210 We characterized ENSO by El Niño and La Niña episodes. The ENSO index positive and negative  
211 episodes correspond to El Niño and La Niña respectively. Consistent with Gabriel and Robock (2015),  
212 ENSO episodes were identified as departures of at least 0.5 standard deviations from zero in a five-  
213 month running averaged ENSO time series. Each episode was characterized by its duration (years),  
214 the extreme peak excursion (°C), and the width at half extreme height (years).

215





216

217 **Figure 1.** AMO (panels a-f), NAO (panels g-l), ENSO (i.e., NINO3.4, panels m-r), and PDO (panels s-x)

218 indices obtained from ensemble members r1(left column), r2 (middle column), and r3 (right

219 column) of the SSP5-8.5 (odd rows) and SSP5-8.5-SAI (even rows) scenarios.

220

221



### 222 2.3. Spatio-temporal analyses

223 Analyses in both space and time as well as modes of variability ranging from the inter-annual through  
224 decadal, to inter-decadal changes were used to identify the possible changes in the large-scale climate  
225 circulations resulting from global warming and SAI scenarios. EOF analysis is commonly used to  
226 extract the climate variability space-time modes (e.g., Chen and Tung, 2018; Joyce, 2002). We applied  
227 EOF to extract the first (dominant) modes of de-trended non-seasonal-SST and its corresponding  
228 variance across the North Atlantic and North Pacific, which are related to the AMO and PDO  
229 respectively. As ENSO is the primary indicator of global climate variability, we used the leading EOF  
230 of global SST anomalies in the study of ENSO.

231 The continuous wavelet transform (CWT) is commonly used to capture the primary characteristics  
232 of signals (Addison, 2018). For a time series  $(x_n, n=1, \dots, N)$  having regular time intervals  $\delta t$ , the  
233 CWT is computed as the convolution of  $x_n$  with the scaled and normalized wavelet (e.g., here we use  
234 the Morlet wavelet which gives reasonably equal weighting and resolution in time and period space;  
235 Grinsted et al., 2004):

$$236 \quad W_n^x(s) = \sqrt{\frac{\delta t}{s}} \sum_{n'=1}^N x_{n'} \psi_0 \left[ (n' - n) \frac{\delta t}{s} \right], \quad \psi_0(\eta) = \pi^{-1/4} e^{i\omega_0 \eta} e^{-0.5\eta^2} \quad (1)$$

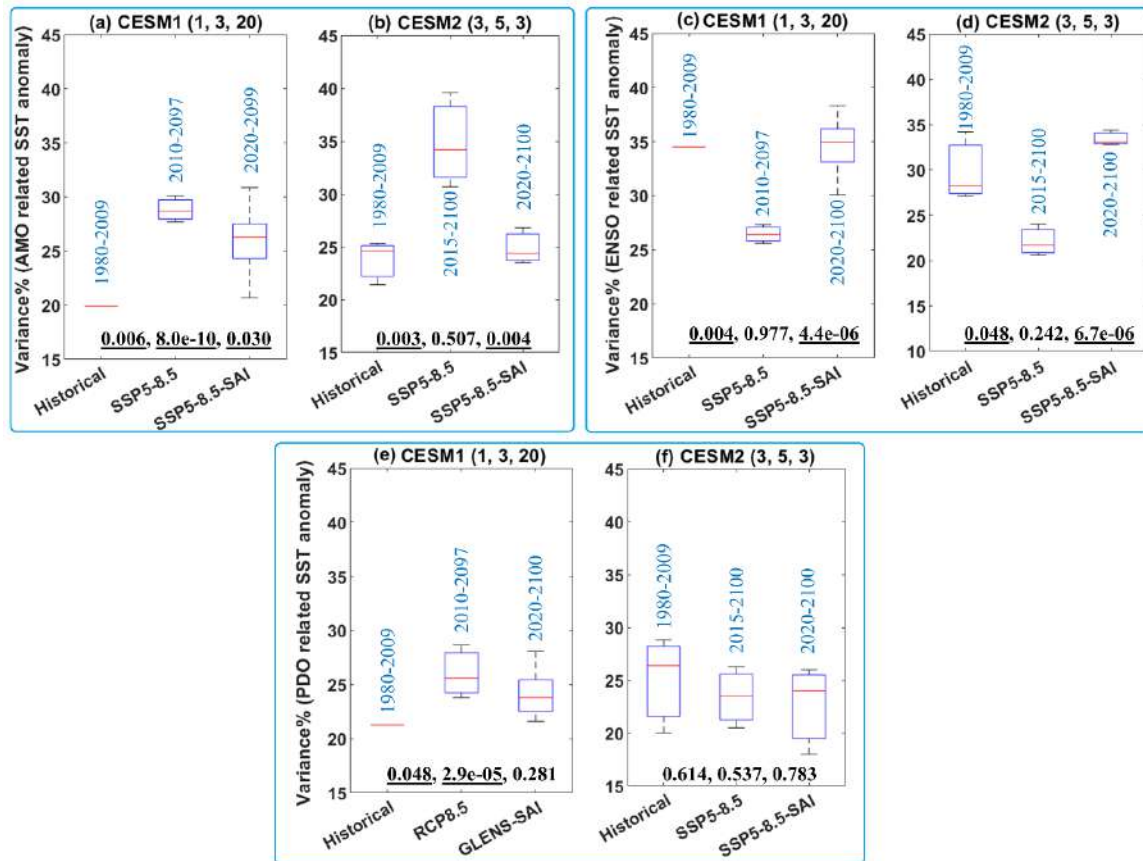
237 where  $s$  is the wavelet scale,  $\psi_0$  the Morlet wavelet,  $\omega_0$  dimensionless frequency,  $[*]$  the complex  
238 conjugate, and  $\eta$  dimensionless time. The noise spectrum assigned to generate significance testing  
239 is a key issue in time series analysis. We concurred with the widely-used red-noise null hypothesis  
240 methodology based on 1000 synthetic series with the same mean, standard deviation and first-order  
241 autoregressive coefficient as the target time series produced by Monte Carlo approaches to estimate  
242 the significance of the CWT (Grinsted et al., 2004). Additionally, for each time series, CWT's global  
243 power spectrum was calculated as a function of time. The global power spectrum provides insight  
244 into the dominant temporal modes of variability of each climate index within each ensemble member  
245 for the reference [GHG greenhouse gas](#) and SAI scenarios. [The wavelet method cone of influence](#)  
246 [automatically shows where the periods analyzed are being influenced by the end of the time series.](#)  
247 [Thus, the longest periods can only be reliably assessed for the middle of the time series.](#)

248 The individual ensemble members are treated as independent of each other in calculating the  
249 statistics of the ensembles. The CWT was conducted on monthly ENSO time series, and the 12-month  
250 moving averaged low-pass filtered signals of AMO, NAO, and PDO. We always use the longest  
251 available record length in every ensemble member to gain maximum statistical power to establish  
252 significant differences between experiments.

### 253 3. Results:

#### 254 3.1. Changes in the spatial patterns

255 Figure 4-2 reveals the projected changes in the variance of the SST anomalies related to the AMO (i.e.,  
256 across the North Atlantic), ENSO (i.e., global scale), and PDO (i.e., across the North Pacific) based on  
257 CESM1 and CESM2 results. ~~Fig. S1 shows There are~~ three different plots for the CESM1 as the time  
258 period of the 20-member ensemble for RCP8.5 differ: ensembles 001 to 003 (2010-2097) are longer  
259 than the other 17 ensemble members (2010-2030). For RCP8.5 and SSP5-85 using CESM1 and  
260 CESM2, respectively, the strong ~~GHG greenhouse gas~~-forcing and global warming to the end of the  
261 21<sup>st</sup> century increases the variance of the first EOF SST anomaly in the North Atlantic and North  
262 Pacific (representing AMO and PDO), but reduces the variance of the leading EOF in global SST  
263 anomaly (related to ENSO). ~~Based on the statistical t-test results, the changes in the means imposed~~  
264 ~~by global warming relative to historical are all significant except one case (Fig. 2f). Differences~~  
265 ~~between SAI and historic in CESM2 values of the leading EOF variance of AMO and ENSO are not~~  
266 ~~significant, showing that the significant changes under GHG forcing are effectively reversed by SAI.~~  
267 ~~In contrast, the changes in PDO variance imposed by global warming using CESM1 relative to~~  
268 ~~historical remain significant under SAI. Using CESM2, there is no significant changes in the PDO~~  
269 ~~variance from historical to global warming, or to SAI. SAI in CESM2 effectively restores the projected~~  
270 ~~changes in the leading EOF variance of each index due to greenhouse gas forcing to its historical~~  
271 ~~values. The lack of statistics for the CESM1 historical scenarios prevents firm conclusions for that~~  
272 ~~model.~~



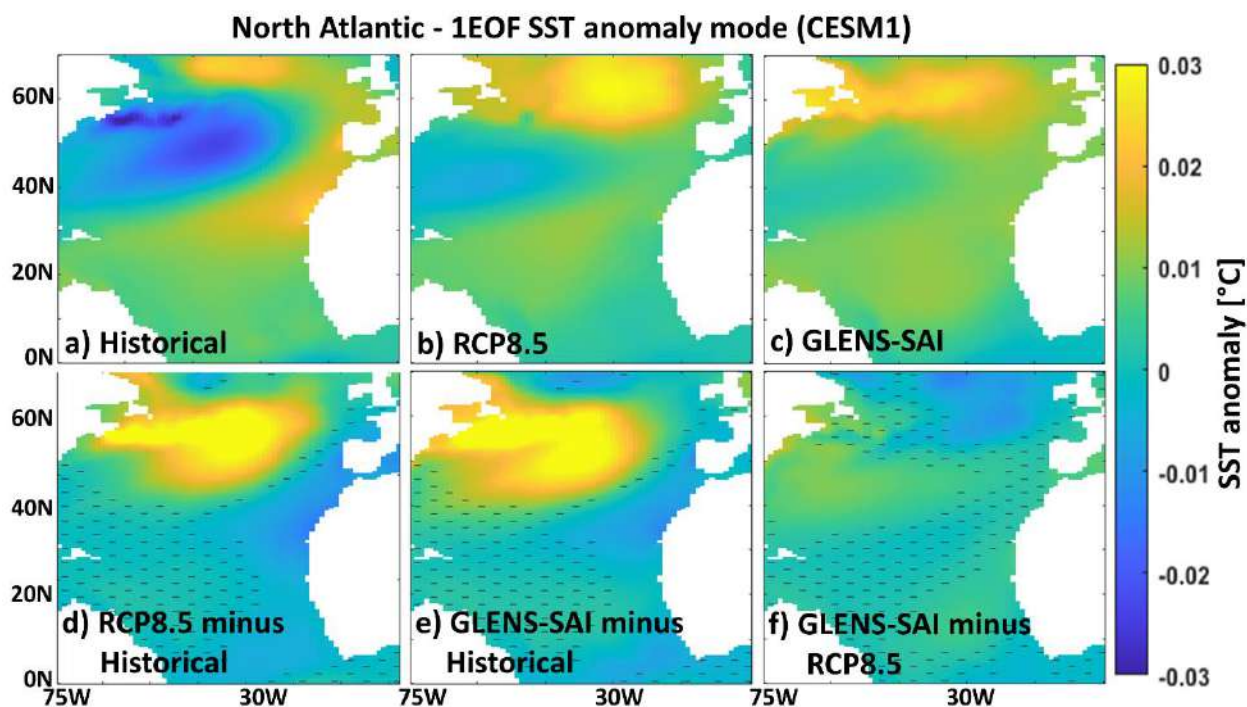
273

274 **Figure 12.** Box and whiskers plot of the variance in the leading EOFs, representing AMO, PDO, and  
 275 ENSO, relative to the total variance of the SST fields: AMO across the North Atlantic (top-left panel);  
 276 ENSO (top-right panel; middle row) global SST; and PDO across the North Pacific (bottom panel; row).  
 277 The values in blue on each column box in the upper row show the period of the data for historical,  
 278 GHG greenhouse gas (i.e., RCP-8.5 and SSP5-8.5), and climate intervention (GLENS-SAI and SSP5-  
 279 8.5-SAI) scenarios. The titles of each subplot refer to the CESM version and the number of  
 280 ensembles used in the historical, GHG greenhouse gas (RCP8.5 and SSP5-8.5), and SAI (GLENS-SAI  
 281 or SSP5-8.5-SAI) scenarios, respectively. The median for each experiment is denoted by the red line,  
 282 the upper (75<sup>th</sup>) and lower (25<sup>th</sup>) quartiles by the top and bottom of the box and ensemble limits by  
 283 the whisker extents. The three values shown at bottom of each sub-plot refer to the p-values  
 284 obtained from the statistical t-test between historical and global warming, historical and SAI, and  
 285 global warming and SAI, respectively. Values underlined are significant (i.e.,  $p < 0.05$ ).  
 286

287 Figures 23-56 and S21-S32 show the spatial anomalies of the leading EOF mode of the SST in the  
 288 North Atlantic, and North Pacific, and tropical Pacific under both the CESM1 and CESM2. For the  
 289 historical period, there is a cold-tongue pattern in the North Pacific broadens from the western to the  
 290 eastern parts surrounded by warm water, particularly to the north. GHG Greenhouse gas-related  
 291 global warming lowers the contrast between the cold-tongue pattern and its surroundings and  
 292 increases the water temperature inside the cold-tongue-pattern, and also leads to a substantial  
 293 expansion of a warm-pattern in the north. The same patterns (shown in Fig. 34) are also obtained

294 under SSP5-8.5 using CESM2. SAI effectively shrinks the warm pattern in the northern Atlantic under  
 295 the RCP8.5 and SSP5-8.5 through a significant SST decrease, particularly using CESM1 (bottom row  
 296 in Figs. 3 and 4). The SSP5-8.5-SAI experiment increases the temperature contrast in the cold-tongue  
 297 pattern, while the GLENS-SAI does not. The projected changes in the spatial SST patterns across the  
 298 North Atlantic, observed under global warming, are largely significantly suppressed under SAI (Figs.  
 299 3f and 4f). This response of AMO to SAI is compatible with the observed changes in AMO imposed by  
 300 anthropogenic and volcanic aerosols reported by Masson-Delmotte et al. (2021). Anthropogenic and  
 301 volcanic aerosols are understood to have impacted the timing and magnitude of the cold (negative)  
 302 episode in the historical AMO record between the mid-1960s and mid-1990s and succeeding  
 303 warming (Masson-Delmotte et al., 2021). Anthropogenic aerosols have also been suspected as  
 304 impacting historical SSTs elsewhere, particularly the decadal ENSO variability (e.g., Sutton and  
 305 Hodson, 2007; Westervelt et al., 2018).

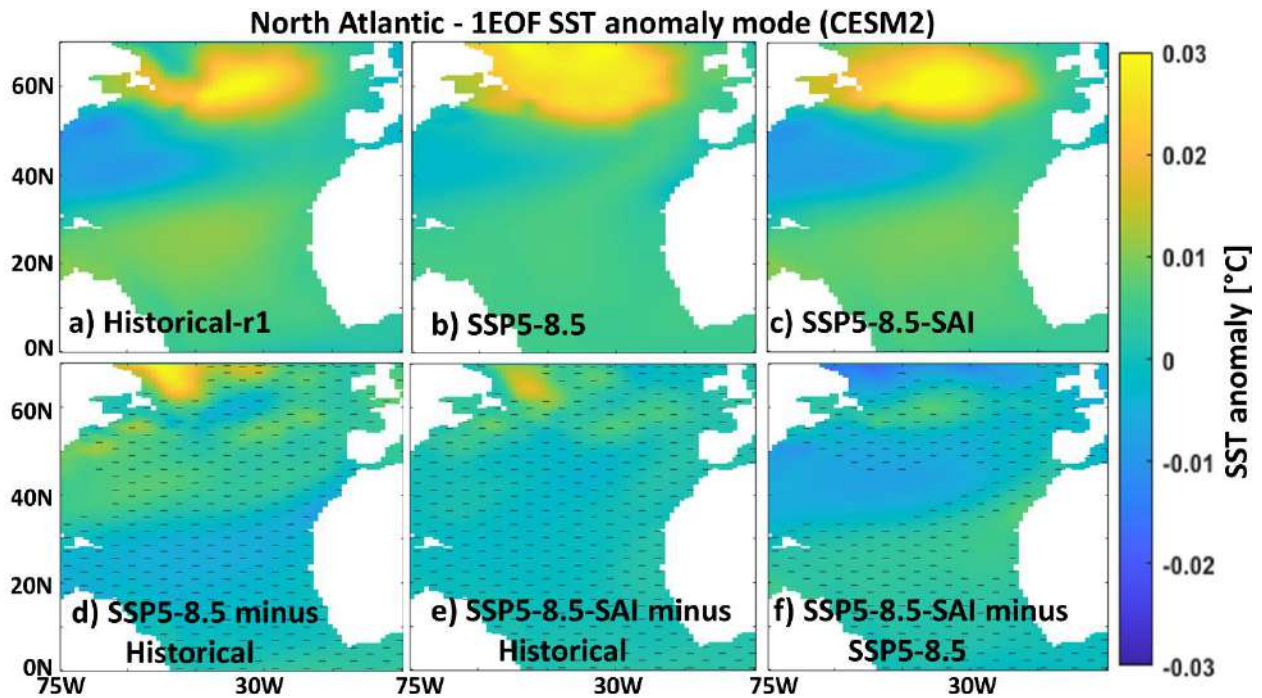
306



307

308 **Figure 3.** The first EOF (1EOF) patterns of SST anomaly across the North Atlantic relate to the AMO  
 309 index simulated by CESM1 for the historical data (a) and the mean of the available ensemble  
 310 members outputs under the RCP8.5 (b) and GLENS-SAI (c) scenarios. The maps at the bottom row  
 311 show RCP8.5 minus historical (d), GLENS-SAI minus historical (e), and GLENS-SAI minus RCP8.5 (f)  
 312 where the hatched patterns are not statistically significant ( $p > 0.05$ ), based on p-values from t-test  
 313 analysis.





314

315

316

**Figure 4.** As in Fig. 3, but for CESM2 and SSP5-8.5.

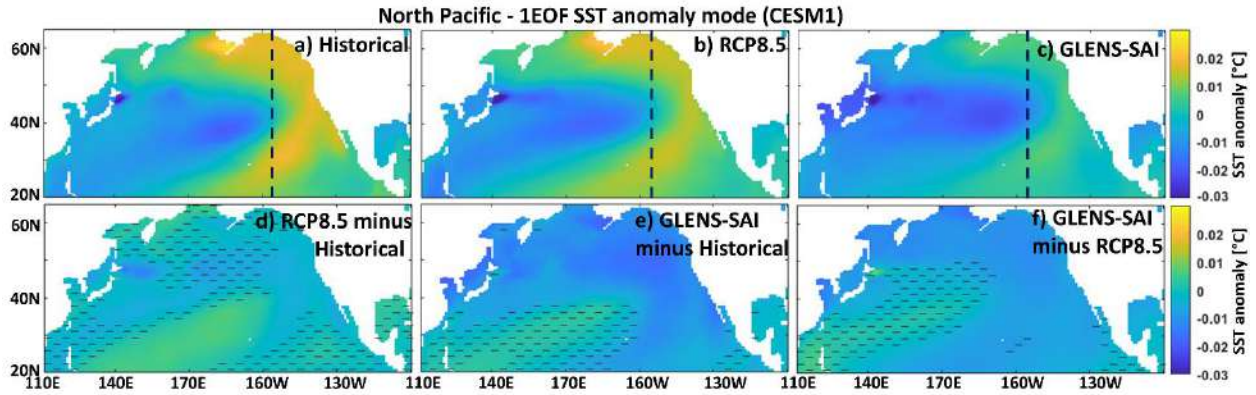
317 The leading EOF of monthly global SST anomalies corresponding to the ENSO mode (Figs. [S1-S2](#) and  
 318 [S3](#)), and is seen as a warm-tongue pattern over the tropical Pacific, that exhibits very similar patterns  
 319 under both global warming and SAI scenarios as in the historical period. However, Fig. [S3-S4](#) shows  
 320 that the warm-tongue pattern in CESM1 and CESM2 has an excessive westward extension relative to  
 321 observations, which is compatible with the findings of Capotondi et al. (2020).

322 While the first EOF SST anomaly across the North Pacific under both global warming and SAI  
 323 scenarios in CESM1 and CESM2 (Figs. [4-5](#) and [5-6](#)) exhibits a similar cold-tongue pattern (typical of  
 324 the North Pacific) as in the historical period, ~~the~~ a lower contrast between the cold-tongue pattern and  
 325 its surroundings is observed under SSP5-8.5 (Fig. [5-6b](#)), which is effectively compensated by the  
 326 geoengineering scenarios of SSP5-8.5-SAI through a significant SST decrease over middle North  
 327 Pacific (Fig. 6c and 6f) since there is no significant change between SAI and historical maps (Fig. 6e).

328 There is an excessive eastward expansion of the cold-tongue pattern with cooler temperatures under  
 329 the SAI scenario as simulated by the CESM1 (Fig. [4-5c](#)), which is due to the significant cooling of the  
 330 water in the outside of the cold-tongue pattern imposed by the SO<sub>2</sub> injection (Fig. [5e-f](#)).

331



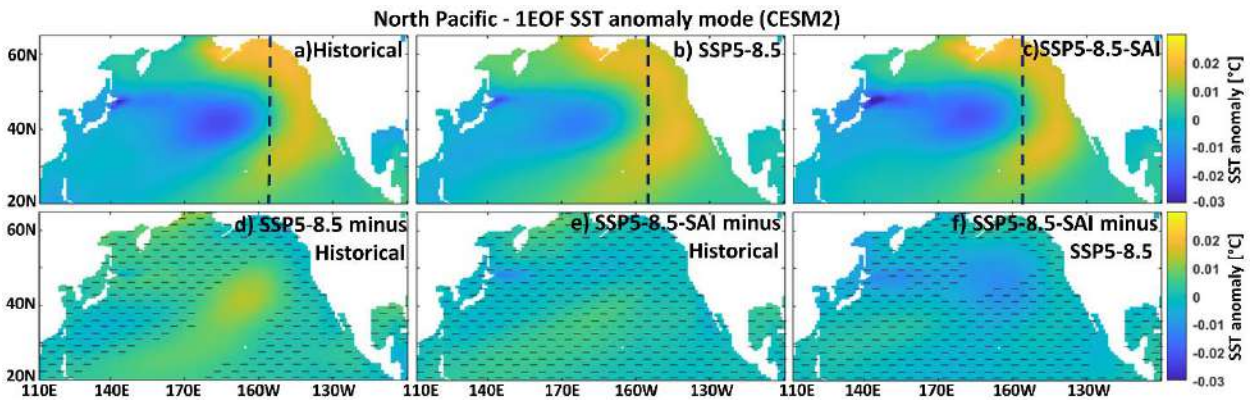


332

333

334

**Figure 5.** As Fig. 3 but across the North Pacific relate to the PDO index.



335

336

337

**Figure 6.** As in Fig. 5, but for CESM2.

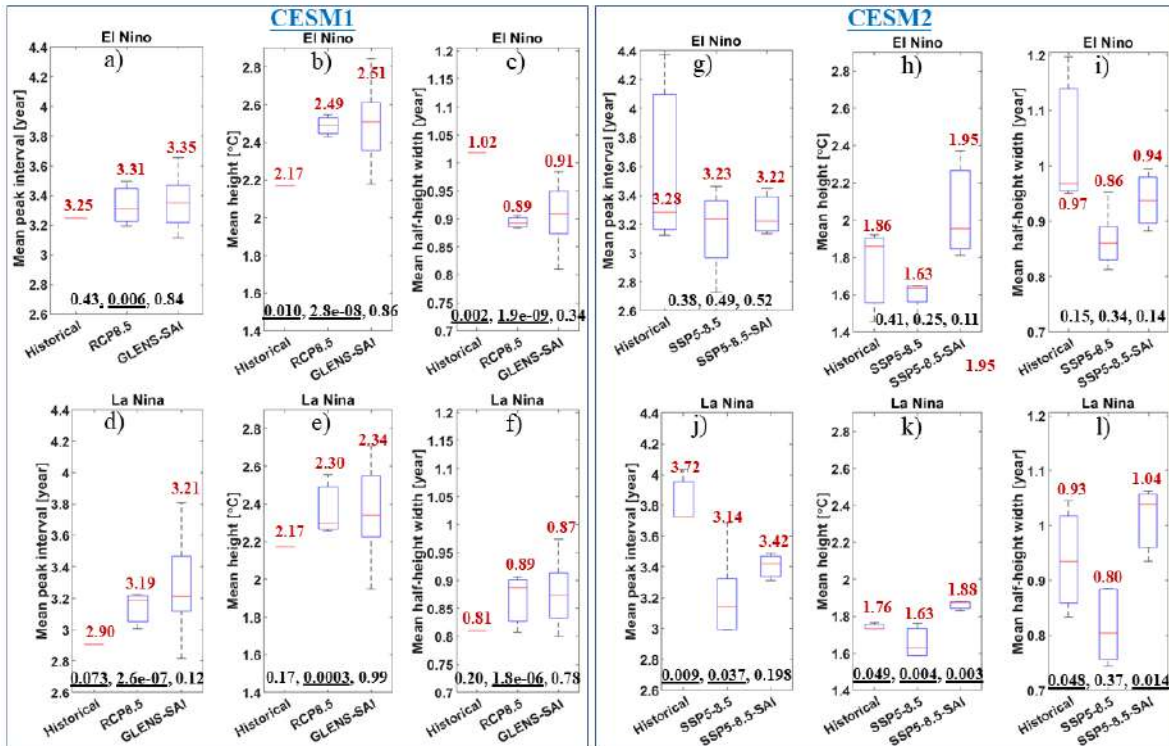
### 3.2. Temporal evolution of indices

339 Figure 67 displays the projected changes in the El Niño and La Niña episodes in the ENSO index under  
 340 global warming and SAI. The global warming scenario simulated by CEMS2 tends to reduce the time  
 341 between, as well as the intensity and duration of the La Niña episodes compared to the historical  
 342 conditions, but El Niño shows no significant changes. Frequency increases in both El Niño and La  
 343 Niña episodes were suggested in earlier climate simulations e.g., Fredriksen et al. (2020), Cai et al.  
 344 (2014) and Yun et al. (2021) for El Niño, and Cai et al. (2015) for La Niña. In contrast, using CESM1,  
 345 the characteristic changes of El Niño are stronger than that of La Niño and the El Niño intensity  
 346 significantly increases while its duration decreases relative to historical period. The La Niño intensity  
 347 significantly increases but other characteristics show no significant changes under RCP8.5. Although  
 348 the global warming scenario simulated by CEMS2 tends to reduce the time between, as well as the  
 349 intensity and duration of the El Niño and La Niña episodes compared to the historical conditions, this

350 is less clear for CESM1. CESM2 results suggest that with greenhouse gases risings, the frequency of  
351 the El Niño and La Niña episodes increases (right panel of Fig. 6), which is supported by earlier  
352 research on climate simulations e.g., Fredriksen et al., (2020); Cai et al. (2014) and Yun et al. (2021)  
353 for El Niño, and Cai et al. (2015) for La Niña. The mean peak interval in CESM2 presented in Fig. 6j  
354 (6g) decreases from 3.72 (3.28) in the historical period to 3.11 (3.20) years for the La Niña (El Niño)  
355 events in the SSP5-85 scenario.

356 Although the SAI is mostly accompanied by a slight decrease in the median of El Niño/La Niña  
357 characteristics towards their historical value, its effect on global warming imposed-changes is only  
358 statistically significant for the intensity and duration of La Niña events. For the CESM2 SAI  
359 experiment, there are no significant differences in El Niño characteristics as with the GHG forcing  
360 experiment. In contrast La Niña peak intervals, height (i.e., intensity), and width (i.e., duration)  
361 characteristics are significantly different from GHG forcing and reverse the direction of changes  
362 imposed by GHG. For CESM1, there are no significant differences between the results from RCP8.5  
363 and GLENS-SAI scenarios. ~~by~~ Nonetheless, for both SAI experiments using CESM1 and CESM2, the  
364 peak intervals, height (i.e., intensity), and width (i.e., duration) of both the El Niño and La Niña  
365 episodes are found to increase relative to the global warming scenarios without SAI, except for La  
366 Niña under CESM1 which shows a small decrease (Fig. 6f). However, while CESM2 provides more  
367 ensemble members over the historical period, SAI tends to compensate for the changes in frequency,  
368 intensity, and duration of the El Niño and La Niña episodes.

369



370

371 **Figure 67.** The projected changes in the mean peak interval, height, and half-height width of El  
 372 Niño and La Niña events for global warming (RCP8.5 and SSP5-8.5) and SAI (GLENS-SAI and SSP5-  
 373 8.5-SAI) scenarios simulated by CESM1 (left panels a-f) and CESM2 (right panel g-l). The median for  
 374 each experiment is denoted by the red line, the upper (75<sup>th</sup>) and lower (25<sup>th</sup>) quartiles by the top  
 375 and bottom of the box and ensemble limits by the whisker extents. The values labeled in red on  
 376 each box show their median. The red flashes are to highlight the effect that SAI has on El Niño and  
 377 La Niña events relative to global warming conditions. The three values shown at bottom of each  
 378 sub-plot refer to the p-values obtained from the statistical t-test between historical and global  
 379 warming, historical and SAI, and global warming and SAI, respectively. Values underlined are  
 380 significant (i.e.,  $p < 0.05$ ).

381

382 Another way to illustrate the temporal evolution of signals is by using the power spectrum. Figures  
 383 7 and 8 and 5S compare the changes in temporal variability of each climate indices (AMO, NAO, ENSO,  
 384 and PDO) using the global power spectrums of CWTs under the global warming and SAI scenarios  
 385 simulated by both the CESM1 and CESM2, excluding CESM1 outputs as there is just a single ensemble  
 386 member for CESM1 historical data over a short 1980-2009 period. In CESM1, the signals longer than  
 387 25 years, which are the most energetic modes in observations of the PDO (Mantua and Hare, 2002)  
 388 and AMO (Enfield et al., 2001), cannot be captured in the historical simulations owing to their short  
 389 simulation period (1980-2009). As an example, Fig. S5 shows the ENSO CWTs and their global power  
 390 spectrums for historical, SSP5-8.5, and SSP5-8.5-SAI scenarios.

391 In CESM1, the dominant mode of AMO in the historical simulation occurs in the 3–5 year band which  
 392 shows no significant change at the 95% level under both global warming and SAI. The historical NAO

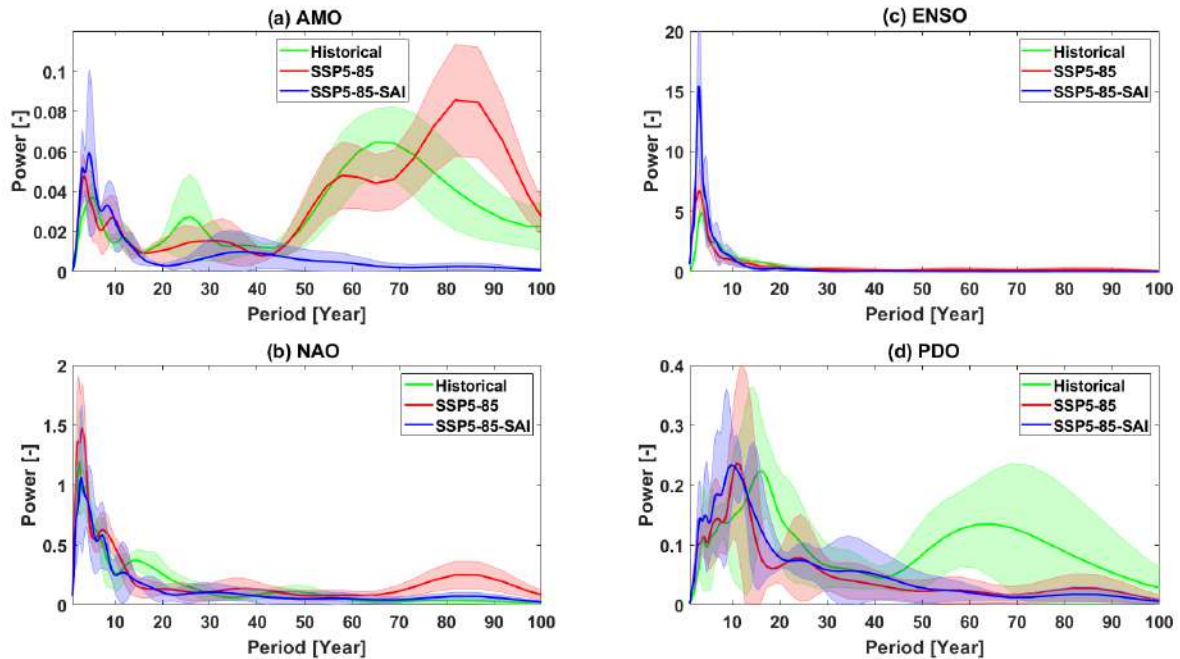
393 ~~has three dominant modes at 1.5 to 4 years (inter-annual), 14 years (decadal), and 21 years (inter-~~  
394 ~~decadal) and which also show no significant change under global warming. The dominant inter-~~  
395 ~~annual mode of NAO is simulated to be preserved under SAI, however, the decadal and interdecadal~~  
396 ~~modes present in the historical simulation and RCP8.5 disappear. For ENSO, the dominant historical~~  
397 ~~inter-annual modes show no significant change under both global warming and SAI. In contrast, the~~  
398 ~~dominant decadal mode disappears under global warming, while SAI does not effectively restore it.~~  
399 ~~Historical PDO also has two dominant modes, at inter-annual (i.e., 3 to 4.5 years) and near decadal (6~~  
400 ~~to 10 years) scales, of which the inter-annual is preserved under both global warming and SAI, but~~  
401 ~~the near decadal mode is greatly weakened under global warming and SAI does not effectively restore~~  
402 ~~it with~~  
403 ~~In CESM1 (Fig. 7), the signals longer than 25 years, which are the most energetic modes in~~  
404 ~~observations of the PDO (Mantua and Hare, 2002) and AMO (Enfield et al., 2001), are not captured in~~  
405 ~~the historical simulations owing to their short simulation period (1980–2009). The historical period~~  
406 ~~simulated by CESM2 (Fig. 8) is long enough (1850–2014) to reasonably capture the low-frequency~~  
407 ~~signals. We therefore consider two different scenarios for the historical period based on CESM2~~  
408 ~~results: 1980–2009 shown in Figs. 8a–8d, upper panel (same as CESM1 (Fig. 7)) and 1850–2014~~  
409 ~~shown in Fig. 8, lower panel.~~  
410 ~~For 1980–2009 (Figs. 8a–8d, upper panel), the inter-annual modes in the historical indices, which is~~  
411 ~~the dominant mode in all climate indices, are preserved under both global warming and SAI, although~~  
412 ~~the power of the historical NAO is considerably smaller than the SSP5-8.5 and SSP5-8.5 SAI NAO (8b).~~  
413 ~~On the contrary, the decadal and inter-decadal signals of the historical climate indices are not~~  
414 ~~preserved in the global warming scenario nor with SAI. Notably, these findings are in agreement with~~  
415 ~~those obtained from the CESM1 (Fig. 7).~~  
416 ~~In comparison with the longer 1850–2014 historical period (Figs. 8e–8h, lower panel), tThe inter-~~  
417 ~~annual modes of AMO, NAO, and ENSO are preserved under both global warming and SAI, consistent~~  
418 ~~with the 1980–2009 period. For the decadal and longer periodicities, SAI accentuates has a counter-~~  
419 ~~productive impact on AMO and NAO changes induced by GHG greenhouse gases (Figs. 8a<sub>e</sub> and 8f).~~  
420 ~~For example, the dominant modes at 20-30- and 55-85-year of the AMO, observed during the~~  
421 ~~historical period, show no significant changes under global warming; however, they vanish under SAI~~  
422 ~~(Fig. 8e). The decadal 10-20-years mode of the historical NAO is not preserved in the global warming~~  
423 ~~scenario nor with SAI (Fig. 8b). Furthermore, the dominant 35–55-year mode in historical NAO is~~  
424 ~~roughly preserved under global warming forcing (but with greater power) while it disappears under~~  
425 ~~SAI (Fig. 8f). For ENSO, the dominant historical inter-annual modes show no significant change under~~



426 both global warming and SAI, except that its power under SAI is stronger (Fig. 8c). The dominant  
427 modes at 10-20- and 50-70-years, observed in historical PDO (consistent with the real PDO's  
428 dominant modes (Mantua et al., 1997)), are not ~~preserved-present under~~ in both the SSP5-8.5 and SAI  
429 simulations, and the latter two are similar to each other ~~global warming and SAI does not impact~~  
430 ~~them~~ (Fig. 8**d**). In contrast with the historical period in which the dominant modes of PDO occur in  
431 the 10-20- and 50-70-year bands, the dominant modes under global warming (i.e., SSP5-8.5) and SAI  
432 (i.e., SSP5-8.5-SAI) occur at the ~10-year period. The PDO shift to a higher frequency with  
433 decadal/multi-decadal variability weakness, observed under global warming, was also earlier  
434 demonstrated by Fang et al. (2014) with a previous generation of the climate model, the Fast Ocean  
435 Atmosphere Model (FOAM) used in IPCC AR4 experiments. Likewise, the PDO timescale has been  
436 simulated to decrease from ~20 to ~12 years under global warming (Fedorov et al., 2020), possibly  
437 because of changes in the phase speed of internal Rossby waves and ocean stratification (Zhang and  
438 Delworth, 2016). Nonetheless, although PDO cycles between 30-50-year bands show slightly  
439 stronger power under SAI than global warming, the 30-50-year is not the dominant PDO mode under  
440 SAI in contrast to Zhang and Delworth's (2016) results for cooler climates, which the PDO dominant  
441 variability shifts to lower frequency (~34 yr). They related this increase to weaker ocean  
442 stratifications accompanied by global cooling. However, Zhang and Delworth (2016) used a different  
443 model (Geophysical Fluid Dynamics Laboratory coupled model version 2.5 through the forecast-  
444 oriented low ocean resolution version) and experiments (2×CO<sub>2</sub> for global warming and 0.5×CO<sub>2</sub> for  
445 cooling).

446 We further analyzed the concatenated series from the available members for each scenario using  
447 CESM2 to statistically capture the low frequency cycles with better reliability. Figure S56 summarizes  
448 the CWT global power spectrums for AMO, NAO, ENSO, and PDO. The results, on the whole, are  
449 compatible with those shown in Fig. 8, despite small discrepancies such as the much stronger  
450 interdecadal mode in AMO obtained from the concatenated ensembles.





451

452 **Figure 8.** As Fig. 7 but for CESM2 under SSP5-8.5 and SSP5-8.5-SAI relative to the historical results  
 453 for the periods of 1980-2009 (upper panel; a to d) and 1850-2014 (lower panel; e to h). The inset  
 454 figure in NAO (b and f) magnifies the historical data. Shading in each curve shows the across-  
 455 ensemble range.

456 **Figure 8.** The CWT global power spectrums obtained for the indices of AMO (a), NAO (b), ENSO (c),  
 457 and PDO (d) under SSP5-8.5 and SSP5-8.5-SAI relative to the historical results based on CESM2 for  
 458 the periods of 1850-2014. Shading in each curve shows the across-ensemble range.

459

## 460 4. Discussion

### 461 4.1. Caveats to interpretation

462 Caution is required when interpreting the results from this study with regard to real-world  
 463 variability. Although CESM2 is highly rated among existing climate models, large model-observation  
 464 differences are nonetheless present (Fasullo, 2020). Model-observation differences are larger in the  
 465 earlier CESM1 version than in CESM2. For example, CESM1 exhibited a Subtropical (Azores) high  
 466 anomaly (related to NAO) that was too weak but its representation is improved in CESM2 (Simpson  
 467 et al., 2020). We also find large differences in amplitude and variance of climate indices simulated by  
 468 both CESM1 and CESM2 relative to the observations over the 1980-2009 period. The amplitude of  
 469 the dominant EOF of the ENSO-related SST-anomaly modeled in both CESM1 and CESM2 is about  
 470 twice the observations for the historical (1980-2009) period (Figs. S3-S4 and S4-S7). Figure S4-S7  
 471 further shows NAO and PDO dominant mode amplitudes are lower in the model projections than in  
 472 observations over the historical period. Additionally, the ENSO-associated SST anomaly pattern in

473 the tropical Pacific shows an excessive westward extension under both CESM1 and CESM2 (Fig. S4).  
474 These limitations mirror those by Capotondi et al. (2020) for CESM2 in simulating the ENSO, who  
475 suggested further work to illuminate how the physical parameterizations impact the key ENSO  
476 feedback. Additionally, although CESM2 simulates the pattern of the summer and winter NAO well  
477 over the historical period 1979-2014, the large uncertainties in specific members and in the historical  
478 observations mean it is difficult to be quantitative about this (Simpson et al., 2020). However, CESM1  
479 tends to underestimate the observed SST fluctuations in the Atlantic, leading to an underestimation  
480 of the forced response (Undorf et al., 2018).

481 CMIP models tend to systematically underestimate the low-frequency signals (i.e., PDO) in the North  
482 Pacific (Fasullo et al., 2020), owing in part to an imperfect modeling of decadal-scale structures in  
483 these simulations (Masson-Delmotte et al., 2021). Compared to observational estimates, the decadal  
484 variability in the subpolar North Atlantic SST appears to be slightly intensified through CMIP6  
485 (Masson-Delmotte et al., 2021). How well we, therefore, can potentially capture forthcoming changes  
486 in climate indices' variability will be restricted by how well-good each model simulatessimulations  
487 are (Gabriel and Robock, 2015).

488 The second limitation is disparities in the length of records (30 years for the historical period, roughly  
489 90 years for GHG emissionsgreenhouse-gas, and 80 years for SAI scenarios) may hinder the direct  
490 comparison of climate indices behavior between historical and future climate scenarios of global  
491 warming and SAI; and thus, the number of El Niño/La Niña events as well as the significance of the  
492 longer periodicities (i.e., decadal and inter-decadal) in power spectrums. Furthermore, these records  
493 explore variability within the statistical assumptions of the methods, which may not be robust for  
494 non-stationary time series where the Normality and independence assumptions inherent in the  
495 wavelet and t-tests would not strictly hold. We are limited to the available simulations, and a 3-  
496 member ensemble for SAI under CESM2 is inherently weaker than 20-member ensembles under  
497 CESM1. CESM1 has a shorter 30-year historical period from 1980 to 2009 which could not capture  
498 the interdecadal variability modes of the teleconnection patterns.

499 Yet another limitation arises from the relatively low spatial resolution of the models which may affect  
500 the spatial SST anomaly patterns. Furthermore, Holmes et al. (2019) pointed out the models are too  
501 low resolution to resolve ocean eddies, which substantially contribute to ENSO irregularity and  
502 predictability. The absence of the eddy process may also be associated with bias in spatial patterns  
503 and other ENSO characteristics (Bellenger et al., 2014) in the CMIP models (Cai et al., 2021). Global  
504 high-horizontal resolution climate models have been indicated to significantly improve the ocean-  
505 atmosphere circulations such as ENSO (Masson et al., 2012). As an example, Haarsma et al. (2016)

506 pointed out that the High Resolution Model Intercomparison Project for CMIP6 improves the  
507 understanding of the climate teleconnection patterns of large-scale circulations such as ENSO, NAO,  
508 and PDO, which suggests that running these high-resolution models with SAI scenario would be  
509 worthwhile.

510

#### 511 **4.2. Implications for climate stability**

512 Teleconnection signals represent emergent properties of the non-linear climate system. The  
513 behavior of the climate teleconnection patterns can be characterized via its oscillations. In its  
514 simplest form, a stable pattern would represent a fixed point or a periodic oscillation, but with real  
515 non-linear systems, a quasi-periodic oscillation over specific frequency bands is usual more likely  
516 (e.g., Ghil et al., 2002). These quasi-periodic characteristic frequencies may change smoothly over  
517 time in a linear system but may proceed towards chaotic solutions via frequency doubling (~~the so-~~  
518 ~~called “Devil’s staircase”~~) in non-linear systems. Moron et al. (1998) suggested that ENSO crossed a  
519 threshold in the early 1960s, and the periodicity of the seasonally forced climatic oscillator increased  
520 abruptly jumped from one stage of the Devil’s staircase to another. The notable decline in low-  
521 frequency multi-decadal band components of the wavelet spectra of the ~~teleconnection~~ indices we  
522 study, accompanied by a concomitant increase in the variance of the decadal band is consistent with  
523 abrupt frequency doubling. This can be expected in non-linear systems as the energy in the system is  
524 raised, progressing along the pathway towards chaotic behavior and hence less predictability on  
525 decadal timescales. Ocean stratification (ocean buoyancy frequency) and the baroclinic Rossby wave  
526 in the North Pacific play significant roles in SST amplitude and PDO cycles since enhanced ocean  
527 buoyancy frequency speeds up the Rossby waves, and so the decadal and longer cycle weakening  
528 accompanies higher PDO frequency (Fang et al., 2014). Ocean stratification changes predominantly  
529 in response to changes in surface temperature and salinity (Fang et al., 2014). The North Atlantic and  
530 the northeast Pacific are projected to be among those areas with the greatest stratification changes  
531 under global warming in the second-half of the 21<sup>st</sup> century (Capotondi et al. 2012). Historical  
532 records also show that volcanic sulfate aerosols have altered multi-decade SST variability in the  
533 North Atlantic and North Pacific (Birkel et al., 2018).

534 Whether the climate system in the model is representative of the earth can be diagnosed to some  
535 extent by comparison of the historical simulation with observations. As noted in Section 4.1 both  
536 CESM versions do present differences from observations, so they are not perfectly clearly simulating a  
537 system that is different from real climate in some ways. All climate models are unavoidably uncertain  
538 (Knutti et al., 2002), mostly because of the imperfect understanding of many of the interplays and

539 feedbacks within the climate system (Jun et al., 2008). Previous analysis of ENSO under SAI found no  
540 significant changes (Gabriel & Robock, 2015), but they used different models with widely varying  
541 fidelity of modeled ENSO to actuality observations, and much smaller simulated quantities of SO<sub>2</sub> with  
542 the relatively modest RCP4.5 emissions scenario as a baseline. Furthermore, in the only previous  
543 assessment of ENSO under SAI, by Gabriel and Robock (2015), SAI simulations may not have been  
544 long enough to detect changes. The large 20-member ensemble of GLENS used in this study may  
545 overcome this limitation, especially for short-period indices, since this represents ~1600 model-  
546 years.

547 Changes in climate teleconnection patterns can indicate significant changes in the forcing conditions  
548 ~~—that is define what forcing is large enough to change the basic response of the system.~~ Such changes  
549 are seen in time series analysis of teleconnection indices in the real world that coincide with  
550 increased GHG greenhouse gases (Tsonis et al., 2007; Wang et al., 2009). Wang et al (2009) note that  
551 regime shifts in system behavior in the observations occurred when North Pacific and North Atlantic  
552 patterns increase their coupling, and the key instigator is the NAO. The NAO's ~~and its~~ long-period  
553 counterpart, the AMO, are seen in our simulations to change under SAI relative to GHG greenhouse  
554 gas forcing at periods longer than a decade. The historical NAO's decadal mode which vanished under  
555 global warming is not restored by the simulated SAI.

556 The North Atlantic is an atypical region under SAI. The declines in heat transported northwards by  
557 the AMOC under GHG greenhouse gas forcing are, to great extent, reversed under all kinds of SRM  
558 including SAI (Xie et al., 2022). Thus, great differences exist in SST and air/ocean heat flux between  
559 SAI and GHG greenhouse gas climates in the North Atlantic (Yue et al., 2021). If regime shifts occur  
560 when North Atlantic and Pacific oceans increase their coupling, and if the decline in AMOC under GHG  
561 greenhouse gas forcing decreases coupling between the basins, then SAI may act to promote regime  
562 shift by reversing a decline in AMOC.

563 Many authors have noted that explosive volcanism, in some ways a natural analogue for SAI, is  
564 accompanied by a positive episode of the NAO (e.g., Robock, 2000), and this may then be associated  
565 with changes in multi-decadal AMO variability (Birkel et al., 2018). Furthermore, in the extreme  
566 scenario of SAI being done such that temperatures are actually decreased then ~~the~~ projected  
567 strengthening of AMOC occurs (Tjiputra et al., 2016). However, it is also possible that regime shifts  
568 induced by GHG greenhouse gas forcing and the large temperature feedbacks they induce may  
569 dominate impacts over those ~~from~~ fairly subtle regime shifts in climate teleconnection patterns.  
570 ~~Which one may be “preferable” for humanity and other species remains an open question.~~

571

## 572 5. Conclusions

573 This study delivers a first overview of SAI response on the large-scale ocean-atmosphere circulations  
574 of AMO, NAO, ENSO, and PDO using experiments based on CESM1(WACCM) and CESM2(WACCM6)  
575 that apply stratospheric aerosol intervention through the injection of sulfur into the stratosphere,  
576 GLENS-SAI and SSP5-8.5-SAI, respectively. The impacts of these interventions are assessed against  
577 historical (1980-2009 ~~for both the models and 1850-2014 for CESM2 in some analyses~~) and  
578 projections under RCP8.5 and SSP5-85 (for the GLENS-SAI and SSP5-8.5-SAI, respectively). We found  
579 that SAI effectively reverses the global warming-imposed changes in the variance of the leading EOF  
580 SST anomaly associated with AMO, ENSO, and PDO. The SAI also effectively suppresses the changes  
581 in the spatial patterns of the EOF SST anomaly across the North Atlantic (i.e., AMO) and North Pacific  
582 (i.e., PDO). A decrease in the contrast between the cold-tongue pattern and its surroundings in the  
583 North Pacific is further projected under ~~GHG greenhouse gas~~-induced global warming, which the SAI  
584 successfully restored.

585 CESM2 simulations suggest that increasing ~~GHG greenhouse gas~~-emissions are accompanied by an  
586 ~~modest~~ increase in the frequency of the El Niño and La Niña episodes but a ~~modest~~ decrease in their  
587 intensity and duration. The SAI scenario effectively compensates for these changes.

588 In contrast to the impact of the SAI on the spatial patterns of the climate indices of AMO, PDO, and  
589 ENSO, the SAI scenario does not effectively suppress the projected changes in decadal and inter-  
590 decadal variability imposed by global warming. The decadal and inter-decadal variability modes of  
591 all the historical climate indices (except for Atlantic-based indices under SSP5-8.5) are not preserved  
592 in the ~~GHG greenhouse gas~~-warming scenario and the SAI does not ~~impact restore~~ them.

593 Furthermore, compared to the historical 1850-2014 period in CESM2, SAI is projected to  
594 ~~accentuate~~~~have a counter-productive impact on~~ AMO and ~~no effective impact on~~ NAO at decadal and  
595 longer frequencies. Unlike the historical period in which the long-period dominant modes of PDO  
596 occur in the 10-20- and 50-70-year bands, the dominant modes under global warming are reduced  
597 to ~10-years, and the SAI does not restore them.

598 The results exhibited here are particular to these types of future global warming scenarios and the  
599 details of the SAI application, which deal with an extreme scenario of ~~GHG greenhouse gas~~-emissions  
600 and continuous increases in sulfur emissions. Furthermore, the findings are from ensemble members  
601 from just two closely related models. Caution is ~~warranted~~ due to the model-observation differences,  
602 disparities in the record length of the historical period compared to future climate scenarios, and the  
603 low spatial resolution of the models. To improve trust in the projected changes and effects of SAI on  
604 the ocean-atmosphere simulations, it is essential to further unravel the primary physical mechanisms



605 behind these changes. Nevertheless, our study does detect changes in [climate](#) teleconnection signals,  
606 and hence underlying climate system dynamics under SAI when decomposed using EOF and wavelet  
607 analyses.

608

#### 609 **Acknowledgments:**

610 We appreciate the financial support from The World Academy of Sciences (TWAS) under grant no:  
611 4500443035. We further thank Gary Strand from NCAR for his help in accessing the CESM1 model  
612 outputs. Tan Mou Leong provided helpful comments and suggestions on the manuscript.

613

#### 614 **Competing interests:**

615 [We confirm that there is no conflict of interest among the authors of this manuscript.](#)

616

#### 617 **Data availability:**

618 [The data for CESM1 and CESM2 simulations are publicly available via their websites:](#)  
619 <http://www.cesm.ucar.edu/projects/community-projects/GLENS/> (DOI: 10.5065/D6JH3JXX) and  
620 <https://esgf-node.llnl.gov/search/cmip6/>.

621

#### 622 **Author contribution:**

623 [A. R.: Coordinated to analysis and the graphics of various figures and the manuscript preparation; Kh.](#)  
624 [K. and S. T.: conceptualization and preparing the data; J. M. conceptualized and coordinated the](#)  
625 [interpretation and discussion for various sections. All authors contributed to the discussion and](#)  
626 [writing.](#)

627

628

#### 629 **References:**

630 Addison, P. S. (2018). Introduction to redundancy rules: the continuous wavelet transform comes of  
631 age. *Philosophical Transactions of the Royal Society A: Mathematical, Physical and*  
632 *Engineering Sciences*, 376(2126), 20170258.

633 [Abdelmoaty, H. M., Papalexiou, S. M., Rajulapati, C. R., & AghaKouchak, A. \(2021\). Biases beyond the](#)  
634 [mean in CMIP6 extreme precipitation: A global investigation. \*Earth's Future\*, 9\(10\),](#)  
635 [e2021EF002196.](#)

636 An, S. I., & Wang, B. (2000). Inter-decadal change of the structure of the ENSO mode and its impact on  
637 the ENSO frequency. *Journal of Climate*, 13(12), 2044-2055.

638 Bellenger, H., Guilyardi, É., Leloup, J., Lengaigne, M., & Vialard, J. (2014). ENSO representation in  
639 climate models: From CMIP3 to CMIP5. *Climate Dynamics*, 42(7), 1999-2018.

640 Birkel, S. D., Mayewski, P. A., Maasch, K. A., Kurbatov, A. V., & Lyon, B. (2018). Evidence for a volcanic  
641 underpinning of the Atlantic multidecadal oscillation. *NPJ Climate and Atmospheric Science*,  
642 1(1), 1-7.

643 Cai, W., Santoso, A., Collins, M., Dewitte, B., Karamperidou, C., Kug, J. S., ... & Zhong, W. (2021).  
644 Changing El Niño–Southern Oscillation in a warming climate. *Nature Reviews Earth &*  
645 *Environment*, 2(9), 628-644.

646 Cai, W., Wang, G., Santoso, A., McPhaden, M. J., Wu, L., Jin, F. F., ... & Guilyardi, E. (2015). Increased  
647 frequency of extreme La Niña events under greenhouse warming. *Nature Climate*  
648 *Change*, 5(2), 132-137.

649 Cai, W., Borlace, S., Lengaigne, M., Van Rensch, P., Collins, M., Vecchi, G., ... & Jin, F. F. (2014). Increasing  
650 frequency of extreme El Niño events due to greenhouse warming. *Nature climate*  
651 *change*, 4(2), 111-116.

652 Capotondi, A., Deser, C., Phillips, A. S., Okumura, Y., & Larson, S. M. (2020). ENSO and Pacific decadal  
653 variability in the Community Earth System Model version 2. *Journal of Advances in Modeling*  
654 *Earth Systems*, 12(12), e2019MS002022.

655 Capotondi, A., & Sardeshmukh, P. D. (2017). Is El Niño really changing?. *Geophysical Research*  
656 *Letters*, 44(16), 8548-8556.

657 Capotondi, A., Alexander, M. A., Bond, N. A., Curchitser, E. N., & Scott, J. D. (2012). Enhanced upper  
658 ocean stratification with climate change in the CMIP3 models. *Journal of Geophysical*  
659 *Research: Oceans*, 117(C4).

660 Chen, X., & Tung, K. K. (2018). Global-mean surface temperature variability: Space–time perspective  
661 from rotated EOFs. *Climate Dynamics*, 51(5), 1719-1732.

662 Cheng, L., Trenberth, K. E., Fasullo, J., Boyer, T., Abraham, J., & Zhu, J. (2017). Improved estimates of  
663 ocean heat content from 1960 to 2015. *Science Advances*, 3(3), e1601545.

664 [Cook, B. I., Mankin, J. S., Marvel, K., Williams, A. P., Smerdon, J. E., & Anchukaitis, K. J. \(2020\). Twenty-](#)  
665 [first century drought projections in the CMIP6 forcing scenarios. \*Earth's Future\*, 8\(6\).](#)  
666 [e2019EF001461.](#)

667 Dagon, K., & Schrag, D. P. (2016). Exploring the effects of solar radiation management on water  
668 cycling in a coupled land–atmosphere model. *Journal of Climate*, 29(7), 2635-2650.

669 [Danabasoglu, G., Lamarque, J. F., Bacmeister, J., Bailey, D. A., DuVivier, A. K., Edwards, J., ... & Strand,](#)  
670 [W. G. \(2020\). The community earth system model version 2 \(CESM2\). \*Journal of Advances in\*](#)  
671 [Modeling Earth Systems, 12\(2\), e2019MS001916.](#)

672 Enfield, D. B., Mestas-Nuñez, A. M., & Trimble, P. J. (2001). The Atlantic multidecadal oscillation and  
673 its relation to rainfall and river flows in the continental US. *Geophysical Research*  
674 *Letters*, 28(10), 2077-2080.

675 Eyring, V., Bony, S., Meehl, G. A., Senior, C. A., Stevens, B., Stouffer, R. J., & Taylor, K. E. (2016). Overview  
676 of the Coupled Model Intercomparison Project Phase 6 (CMIP6) experimental design and  
677 organization. *Geoscientific Model Development*, 9(5), 1937-1958.

678 Fang, C., Wu, L., & Zhang, X. (2014). The impact of global warming on the Pacific Decadal Oscillation  
679 and the possible mechanism. *Advances in Atmospheric Sciences*, 31(1), 118-130.

680 [Fasullo, J. T. and Richter, J. H. \(2022\). Scenario and Model Dependence of Strategic Solar Climate](#)  
681 [Intervention in CESM, EGUsphere \[preprint\], <https://doi.org/10.5194/egusphere-2022-779>,](#)  
682 [2022.](#)

683 Fasullo, J. T., Phillips, A. S., & Deser, C. (2020). Evaluation of leading modes of climate variability in  
684 the CMIP archives. *Journal of Climate*, 33(13), 5527-5545.

685 Fedorov, A. V., Hu, S., Wittenberg, A. T., Levine, A. F., & Deser, C. (2020). ENSO Low-Frequency  
686 Modulation and Mean State Interactions. *El Niño Southern Oscillation in a changing climate*,  
687 173-198.

688 Fedorov, A. V., & Philander, S. G. (2001). A stability analysis of tropical ocean-atmosphere  
689 interactions: Bridging measurements and theory for El Niño. *Journal of Climate*, 14(14),  
690 3086-3101.

691 Field, C. B., & Barros, V. R. (Eds.). (2014). *Climate change 2014—Impacts, adaptation and vulnerability:*  
692 *Regional aspects*. Cambridge University Press.

693 Fredriksen, H. B., Berner, J., Subramanian, A. C., & Capotondi, A. (2020). How does El Niño–Southern  
694 Oscillation change under global warming—A first look at CMIP6. *Geophysical Research*  
695 *Letters*, 47(22), e2020GL090640.

696 Gabriel, C. J., & Robock, A. (2015). Stratospheric geoengineering impacts on El Niño/Southern  
697 Oscillation. *Atmospheric Chemistry and Physics*, 15(20), 11949-11966.

698 Ghil, M., Allen, M. R., Dettinger, M. D., Ide, K., Kondrashov, D., Mann, M. E., ... & Yiou, P. (2002).  
699 Advanced spectral methods for climatic time series. *Reviews of geophysics*, 40(1), 3-1.

700 Greene, C. A., Thirumalai, K., Kearney, K. A., Delgado, J. M., Schwanghart, W., Wolfenbarger, N. S., ... &  
701 Blankenship, D. D. (2019). The climate data toolbox for MATLAB. *Geochemistry, Geophysics,*  
702 *Geosystems*, 20(7), 3774-3781.

703 Grinsted, A., Moore, J.C., Jevrejeva, S. (2004). Application of the cross wavelet transform and wavelet  
704 coherence to geophysical time series. *Nonlinear Proc. Geoph.* 11 (5-6), 561-566.

705 Haarsma, R. J., Roberts, M. J., Vidale, P. L., Senior, C. A., Bellucci, A., Bao, Q., ... & von Storch, J. S. (2016).  
706 High resolution model intercomparison project (HighResMIP v1. 0) for CMIP6. *Geoscientific*  
707 *Model Development*, 9(11), 4185-4208.

708 Holmes, R. M., McGregor, S., Santoso, A., & England, M. H. (2019). Contribution of tropical instability  
709 waves to ENSO irregularity. *Climate Dynamics*, 52(3), 1837-1855.

710 Hu, Z. Z., & Wu, Z. (2004). The intensification and shift of the annual North Atlantic Oscillation in a  
711 global warming scenario simulation. *Tellus A: Dynamic Meteorology and*  
712 *Oceanography*, 56(2), 112-124.

713 [Intergovernmental Panel on Climate Change \(IPCC\): 2007. Working Group I Contribution to the Sixth](https://www.ipcc.ch/assessment-report/ar6/)  
714 [Assessment Report \(AR6\), Climate Change 2021: The Physical Science Basis, 2021. Available](https://www.ipcc.ch/assessment-report/ar6/)  
715 [online: https://www.ipcc.ch/assessment-report/ar6/.](https://www.ipcc.ch/assessment-report/ar6/)

716 Joyce, T. M. (2002), One hundred plus years of wintertime climate variability in the eastern United  
717 States, *J. Clim.*, 15, 1076–1086.

718 [Knutti, R., Stocker, T. F., Joos, F., & Plattner, G. K. \(2002\). Constraints on radiative forcing and future](#)  
719 [climate change from observations and climate model ensembles. \*Nature\*, 416\(6882\), 719-](#)  
720 [723.](#)

721 [Jun, M., Knutti, R., & Nychka, D. W. \(2008\). Spatial analysis to quantify numerical model bias and](#)  
722 [dependence: how many climate models are there?. \*Journal of the American Statistical\*](#)  
723 [Association](#), 103(483), 934-947.

724 Kravitz, B., MacMartin, D. G., Mills, M. J., Richter, J. H., Tilmes, S., Lamarque, J. F., et al. (2017). First  
725 simulations of designing stratospheric sulfate aerosol geoengineering to meet multiple  
726 simultaneous climate objectives. *Journal of Geophysical Research: Atmospheres*, 122,  
727 12,616–12,634.

728 Kravitz, B., Caldeira, K., Boucher, O., Robock, A., Rasch, P. J., Alterskjaer, K., ... & Yoon, J. H. (2013).  
729 Climate model response from the geoengineering model intercomparison project  
730 (GeoMIP). *Journal of Geophysical Research: Atmospheres*, 118(15), 8320-8332.

731 Latif, M., & Keenlyside, N. S. (2009). El Niño/Southern Oscillation response to global  
732 warming. *Proceedings of the National Academy of Sciences*, 106(49), 20578-20583.

733 Mantua, N., & Hare, S., (2002). The Pacific Decadal oscillation. *J. Oceanogr.* 58 (1), 35–44.  
734 <http://dx.doi.org/10.1023/A:1015820616384>.

735 Mantua, N. J., Hare, S. R., Zhang, Y., Wallace, J. M., & Francis, R. C. (1997). A Pacific interdecadal climate  
736 oscillation with impacts on salmon production. *Bulletin of the American Meteorological*  
737 *Society*, 78(6), 1069-1080.

738 Masson-Delmotte, V., Zhai, P., Pirani, A., Connors, S. L., Péan, C., Berger, S., ... & Zhou, B. (2021). Climate  
739 change 2021: the physical science basis. Contribution of working group I to the sixth  
740 assessment report of the intergovernmental panel on climate change, 2.

741 Masson, S., Terray, P., Madec, G., Luo, J. J., Yamagata, T., & Takahashi, K. (2012). Impact of intra-daily  
742 SST variability on ENSO characteristics in a coupled model. *Climate dynamics*, 39(3), 681-  
743 707.

744 Mills, M. J., Richter, J. H., Tilmes, S., Kravitz, B., MacMartin, D. G., Glanville, A. A., et al. (2017). Radiative  
745 and chemical response to interactive stratospheric sulfate aerosols in fully coupled  
746 CESM1(WACCM). *Journal of Geophysical Research: Atmospheres*, 122, 13,061–13,078.

747 Meinshausen, M., Lewis, J., McGlade, C., Gütschow, J., Nicholls, Z., Burdon, R., ... & Hackmann, B. (2022).  
748 Realization of Paris Agreement pledges may limit warming just below 2°  
749 C. *Nature*, 604(7905), 304-309.

750 Moore, J. C., Yue, C., Zhao, L., Guo, X., Watanabe, S., & Ji, D. (2019). Greenland ice sheet response to  
751 stratospheric aerosol injection geoengineering. *Earth's Future*, [https://doi.org/10.1029/](https://doi.org/10.1029/2019EF001393)  
752 [2019EF001393](https://doi.org/10.1029/2019EF001393).

753 Moore, J. C., Rinke, A., Yu, X., Ji, D., Cui, X., Li, Y., et al. (2014). Arctic sea ice and atmospheric circulation  
754 under the GeoMIP G1 scenario. *Journal of Geophysical Research: Atmospheres*, 119, 567–583.

755 Moron, V., Vautard, R., & Ghil, M. (1998). Trends, interdecadal and interannual oscillations in global  
756 sea-surface temperatures. *Climate Dynamics*, 14(7), 545-569.

757 Riahi, K., Rao, S., Krey, V., Cho, C., Chirkov, V., Fischer, G., ... & Rafaj, P. (2011). RCP 8.5—A scenario of  
758 comparatively high greenhouse gas emissions. *Climatic change*, 109(1), 33-57.

759 Robock, A. (2000). Volcanic eruptions and climate. *Reviews of Geophysics*, 38(2), 191–  
760 219. <https://doi.org/10.1029/1998RG000054>

761 [Scafetta, N. \(2021\). Testing the CMIP6 GCM Simulations versus surface temperature records from](#)  
762 [1980–1990 to 2011–2021: High ECS is not supported. \*Climate\*, 9\(11\), 161.](#)

763 Simpkins, G. (2021). Breaking down the NAO–AO connection. *Nature Reviews Earth &*  
764 *Environment*, 2(2), 88-88.



765 Simpson, I. R., Bacmeister, J., Neale, R. B., Hannay, C., Gettelman, A., Garcia, R. R., ... & Richter, J. H.  
766 (2020). An evaluation of the large-scale atmospheric circulation and its variability in CESM2  
767 and other CMIP models. *Journal of Geophysical Research: Atmospheres*, 125(13),  
768 e2020JD032835.

769 Shukla, J. (1998). Predictability in the midst of chaos: A scientific basis for climate  
770 forecasting. *science*, 282(5389), 728-731.

771 Sutton, R. T., & Hodson, D. L. (2007). Climate response to basin-scale warming and cooling of the  
772 North Atlantic Ocean. *Journal of Climate*, 20(5), 891–907.

773 Tilmes, S., MacMartin, D. G., Lenaerts, J., Van Kampenhout, L., Muntjewerf, L., Xia, L., ... & Robock, A.  
774 (2020). Reaching 1.5 and 2.0 C global surface temperature targets using stratospheric aerosol  
775 geoengineering. *Earth System Dynamics*, 11(3), 579-601.

776 Tilmes, S., Richter, J. H., Kravitz, B., MacMartin, D. G., Mills, M. J., Simpson, I. R., et al. (2018).  
777 CESM1(WACCM) Stratospheric Aerosol Geoengineering Large Ensemble Project. *Bulletin of*  
778 *the American Meteorological Society*, 99, 2361–2371. [https://doi.org/10.1175/BAMSD-17-](https://doi.org/10.1175/BAMSD-17-0267.1)  
779 [0267.1](https://doi.org/10.1175/BAMSD-17-0267.1).

780 Tjiputra, J. F., Grini, A., & Lee, H. (2016). Impact of idealized future stratospheric aerosol injection on  
781 the large-scale ocean and land carbon cycles. *Journal of Geophysical Research:*  
782 *Biogeosciences*, 121(1), 2-27.

783 Trenberth, K. E. (1997). The definition of El Niño. *Bulletin of the American Meteorological*  
784 *Society*, 78(12), 2771-2778.

785 Tsonis, A. A., Swanson, K., & Kravtsov, S. (2007). A new dynamical mechanism for major climate  
786 shifts. *Geophysical Research Letters*, 34(13).

787 Undorf, S., Bollasina, M. A., Booth, B. B. B., & Hegerl, G. C. (2018). Contrasting the effects of the 1850–  
788 1975 increase in sulphate aerosols from North America and Europe on the Atlantic in the  
789 CESM. *Geophysical Research Letters*, 45(21), 11-930.

790 Wang, G., Swanson, K. L., & Tsonis, A. A. (2009). The pacemaker of major climate shifts. *Geophysical*  
791 *Research Letters*, 36(7).

792 Wang, C., & Dong, S. (2010). Is the basin-wide warming in the North Atlantic Ocean related to  
793 atmospheric carbon dioxide and global warming?. *Geophysical Research Letters*, 37(8).

794 Watson, A. J., Schuster, U., Bakker, D. C., Bates, N. R., Corbière, A., González-Dávila, M., ... & Wanninkhof,  
795 R. (2009). Tracking the variable North Atlantic sink for atmospheric CO<sub>2</sub>. *Science*, 326(5958),  
796 1391-1393.

797 Westervelt, D. M., Conley, A. J., Fiore, A. M., Lamarque, J.-F., Shindell, D. T., Previdi, M., et al. (2018).  
798 Connecting regional aerosol emissions reductions to local and remote precipitation  
799 responses. *Atmospheric Chemistry and Physics Discussions*, 18, 12,461–12,475.  
800 <https://doi.org/10.5194/acp-2018-516>.

801 Xie, M., Moore, J. C., Zhao, L., Wolovick, M., & Muri, H. (2022). Impacts of three types of solar  
802 geoengineering on the Atlantic Meridional Overturning Circulation. *Atmospheric Chemistry  
803 and Physics*, 22(7), 4581-4597.

804 Yue, C., Schmidt, L. S., Zhao, L., Wolovick, M., & Moore, J. C. (2021). Vatnajökull mass loss under solar  
805 geoengineering due to the North Atlantic meridional overturning circulation. *Earth's  
806 Future*, 9(9), e2021EF002052.

807 Yun, K. S., Lee, J. Y., Timmermann, A., Stein, K., Stuecker, M. F., Fyfe, J. C., & Chung, E. S. (2021).  
808 Increasing ENSO–rainfall variability due to changes in future tropical temperature–rainfall  
809 relationship. *Communications Earth & Environment*, 2(1), 1-7.

810 Zhang, L., & Delworth, T. L. (2016). Simulated response of the Pacific decadal oscillation to climate  
811 change. *Journal of Climate*, 29(16), 5999-6018.

812 Zhang, R., & Delworth, T. L. (2006). Impact of Atlantic multidecadal oscillations on India/Sahel  
813 rainfall and Atlantic hurricanes. *Geophysical research letters*, 33(17).